Eur. Phys. J. B **25**, 269–280 (2002)
DOI: 10.1140/epjb/e20020031

THE EUROPEAN PHYSICAL JOURNAL B

EDP Sciences
© Società Italiana di Fisica
Springer-Verlag 2002

Structure and mechanical properties of low stress tetrahedral amorphous carbon films prepared by pulsed laser deposition

M. Bonelli[1], A.C. Ferrari[2], A. Fioravanti[3], A. Li Bassi[3], A. Miotello[1], and P.M. Ossi[3,a]

[1] INFM and Dipartimento di Fisica, Università di Trento, 38050 Povo (TN), Italy
[2] Department of Engineering, University of Cambridge, Cambridge CB2 1PZ, UK
[3] INFM and Dipartimento di Ingegneria Nucleare, Politecnico di Milano, Via Ponzio 34/3, 20133 Milano, Italy

Received 25 June 2001

Abstract. Tetrahedral amorphous carbon films have been produced by pulsed laser deposition, at a wavelength of 248 nm, ablating highly oriented pyrolytic graphite at room temperature, in a 10^{-2} Pa vacuum, at fluences ranging between 0.5 and 35 $\mathrm{Jcm^{-2}}$. Both (100) Si wafers and wafers covered with a SiC polycrystalline interlayer were used as substrates. Film structure was investigated by Raman spectroscopy at different excitation wavelength from 633 nm to 229 nm and by transmission Electron Energy Loss Spectroscopy. The films, which are hydrogen-free, as shown by Fourier Transform Infrared Spectroscopy, undergo a transition from mainly disordered graphitic to up to 80% tetrahedral amorphous carbon (ta-C) above a threshold laser fluence of 5 J $\mathrm{cm^{-2}}$. By X-ray reflectivity roughness, density and cross-sectional layering of selected samples were studied. Film hardness as high as 70 GPa was obtained by nanoindentation on films deposited with the SiC interlayer. By scratch test film adhesion and friction coefficients between 0.06 and 0.11 were measured. By profilometry we obtained residual stress values not higher than 2 GPa in as-deposited 80% sp^3 ta-C films.

PACS. 81.15Fg Laser deposition – 78.30.Ly Disordered solids – 68.60.-p Physical properties of thin films, nonelectronic – 62.20.Qp Tribology and hardness

1 Introduction

Diamond-like carbon (DLC) films are the object of widespread attention from scientists and technologists due to their mechanical and optical properties. These are strongly dependent on the content of sp^3 bonded carbon atoms, on the amount of clustering of the sp^2 phase, on the orientation and anisotropy of the sp^2 phase and on the cross-sectional structure [1,2]. For mechanical applications requiring low friction coefficient and very high hardness, hydrogen-free high sp^3 tetrahedral amorphous carbons are most appealing, though they find one main limitation in the high degree of as-grown compressive stress, which results in thin films not well adhering to the substrates. Ta-C optical transparency in a wide spectral range and absorbance in the UV are promising for scratch resistant thin coatings of lenses.

An interesting technique to deposit a variety of thin films is Pulsed Laser Deposition (PLD). Growth of DLC films from vacuum laser ablated graphite was first reported in 1985 [3], and rapidly proved to be effective for the preparation of hydrogen- free amorphous carbon films [4–7]. Low deposition temperatures, high deposition rates and flexibility are some of the advantages offered by this technique; the degree of diamond-like character considerably varies with deposition parameters, such as vacuum, laser wavelength and fluence, which need therefore to be calibrated. In order to grow relatively hard films by PLD, a vacuum of at least 10^{-4}–10^{-5} Pa seems to be required [4,8–10] and there is general agreement on the existence of a threshold fluence, which increases with laser wavelength ($\approx 3 \times 10^8$ J $\mathrm{mm^{-2}}$ for $\lambda_{\mathrm{laser}} = 248$ nm [11]). The use of UV excimer lasers seems to be preferable to obtain good quality films, since they reduce particulate emission and allow the deposition of ta-C films using lower laser fluences if compared to visible and Infra-red lasers [8–12].

Here we report the preparation of PLD ta-C films and their structural and mechanical characterisation. Our results show that we obtained films with a high content of sp^3 carbon (up to 80%), with an hardness of up to 70 GPa and with a low as-grown compressive stress, working at a vacuum level and fluence lower than those usually reported. A multi-wavelength Raman spectroscopy investigation, for excitation energies of 229, 244, 325, 458, 514.5 and 633 nm has been conducted to characterise the bonding evolution in the films. Fourier Transform Infra-Red spectroscopy (FTIR) was used to further study the structure and to assess the hydrogen content. X-ray reflectivity (XRR) was performed to non-destructively derive film

[a] e-mail: paolo.ossi@polimi.it

Table 1. Collection of relevant data on deposition parameters, structural and mechanical properties of DLC films. The sp^3 content of the samples grown at 0.5 J cm^{-2} and 20 J cm^{-2} were directly measured, the other values are estimates derived by the comparison of the Raman spectra taken at different excitation energy.

Fluence [J/cm^2]	Substrate	Thickness [nm]	Sp^3 [%]	Hardness [GPa]	LC2 [N]	Friction coefficient	Residual stress [GPa]
0.5	Si (100)	120	42	27	8	0.07	0
1.13	Si (100)	400	Low (≈ 40%)	-	20	0.065	0.30
1.7	Si (100)	760	Low (≈ 40%)	32	21	0.09	0.48
2.1	Si (100)	1300	Low (≈ 40%)	-	23	0.08	0.47
4.5	Si (100)	370	-	-	17	0.06	0.92
7	Si (100)	230	High (≈ 70%)	-	18.5	0.077	1.6
9.3	Si (100)	90	High (≈ 70%)	-	14	0.053	1.4
20	Si (100)	130	80	36	18.5	0.07	1.7
31	Si (100)	130	≈ 80	40	20	0.057	2
29	Si(100)+500nm SiC	210	≈ 80	70	14	0.11(*)	1.9
35	Si(100)+250nm SiC	170	≈ 80	65	17	0.066	
35	Si(100)+900nm TiC	135	≈ 80	-	8	0.055	
35	Si(100)+200nm TiN	100	≈ 80	-	<4	-	

(*): Surface roughness about 10 nm.

roughness, density and cross sectional layering. Electron energy loss spectroscopy allowed to quantify the fraction of sp^3 bonded carbon. Nanoindentation was used to measure film hardness and elastic modulus. Scratch tests were performed to study film adhesion to substrates and friction coefficient. Profilometry allowed us to measure the macroscopic film stress.

2 Experimental

A series of films was deposited at an operating pressure of 10^{-2} Pa, from a starting base pressure of 10^{-3} Pa. Highly oriented pyrolytic graphite (HOPG) (purity 99.99%), was ablated with laser pulses from a Lambda Physik LPX220i Excimer Laser (wavelength $\lambda = 248$ nm, pulse duration $\tau = 20$ ns, repetition frequency 10 Hz, incidence angle 45°), with fluence ranging from 0.5 J cm^{-2} to 35 J cm^{-2}. On purpose designed mechanisms moved the graphite target disk in order to avoid formation of craters and to obtain uniform surface ablation [13]. Different types of ultrasonically cleaned substrates were used, as shown in Table 1: we chose Si (100) for structural analysis and Si (100) coated with sputter deposited SiC, or TiC, or TiN for mechanical analysis in order to reduce substrate influence in nanoindentation. Substrate and film thickness, as determined with a DEKTAK IIA profilometer, are reported in Table 1 together with laser fluences. Deposition rates were of the order of 0.6 nm s^{-1}.

Unpolarised Raman spectra were acquired at $\lambda = 229$, 244, 325, 458, 514.5, 633 nm, (5.41–1.96 eV) using a variety of spectrometers [14]. The UV Raman spectra at 229 and 244 nm were excited using an intracavity, frequency-doubled Ar ion laser (Coherent Innova 300 series) and the 325 nm with a He-Cd laser. Fused silica optics were used throughout, and Raman spectra were collected using two Renishaw micro-Raman 1000 spectrometers on a 40X objective, with 229, 244 or 325 nm filters, and an UV-enhanced CCD camera. The spectral resolution was about 4–6 cm^{-1} at 244 and 325 nm, but rose to 12–15 cm^{-1} for 229 nm excitation. All the UV spectra must be corrected by subtracting the system response signal, obtained by measuring a background spectrum with an Al mirror and normalising to the atmospheric N_2 vibrations. Unpolarized visible Raman spectra were recorded in backscattering geometry for 514.5 nm excitation from an Ar ion laser using a Jobin-Yvon T64000 triple grating spectrometer. Another Renishaw system with a 50X objective was used to acquire spectra at 633 nm, from a He-Ne laser, with a resolution of 3–6 cm^{-1}. Care was taken to avoid sample damage.

FTIR spectra were taken at room temperature, in dry air, using a Win-Bio-Rad Fast Transform spectroscope over the 400–4000 cm^{-1} range; the spectra were recorded in transmission and corrected for Si substrate contributions.

EELS measurements were carried out on a dedicated VG501 scanning transmission electron microscope fitted with a spectrometer with a McMullan parallel EELS detection system [15].

Specular X-ray reflectivity (XRR) curves were acquired with a Bede Scientific GIXR reflectometer, equipped with a Bede EDRa scintillation detector, using the Cu K$_\beta$ radiation ($\lambda = 0.13926$ nm). Off-specular curves were subtracted from specular curves to get real specular data, with the incidence angle θ_i usually varying in the range 0–8000 arcseconds, with a step of 15 arcseconds.

The macroscopic stress of the films deposited on Si was determined by Stoney's equation [16], measuring the substrate curvature before and after film deposition by a UBM Messtechnik Laser Microfocus profilometer.

Film hardness was determined by a Nano Instruments (type II) ultra low load depth-sensing nanoindenter (ind. depth 50 nm); data were analysed by the Oliver-Pharr procedure [17].

Film-substrate adhesion was tested by scratch tests, performed with a CSEM Revetest Automatic Scratch-Tester equipped with a Rockwell shaped diamond indenter (conical angle 120°, hemispherical tip of 100 μm radius), at a scratching speed of 10 mm min^{-1} and a loading rate of 10 N mm^{-1}.

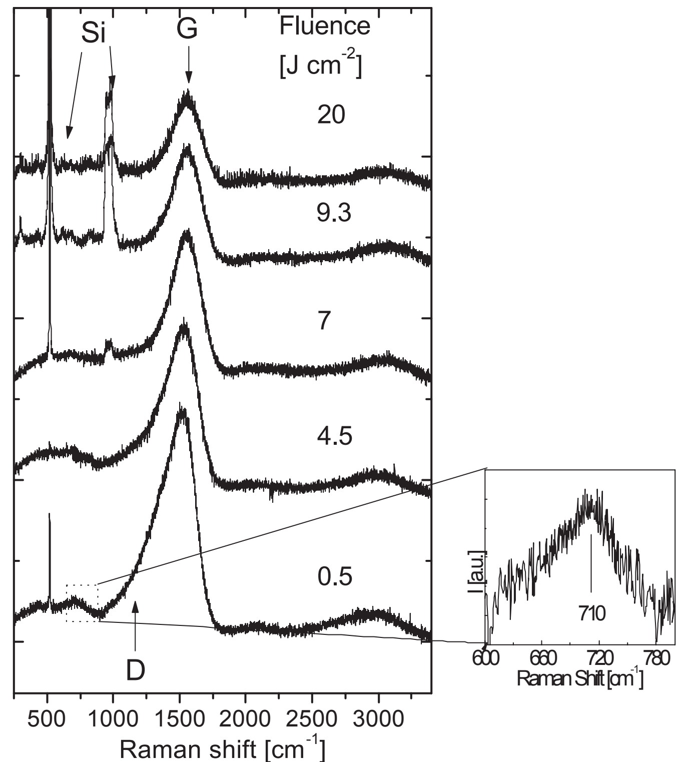

Fig. 1. 514.5 nm Raman spectra for a selection of samples grown at various fluences. The inset shows the typical broad band centred around 710 cm^{-1} in films deposited below f_t.

3 Results

3.1 Raman spectroscopy

Raman spectroscopy is a very popular, non-destructive tool for the structural characterization of carbons. Raman scattering from carbons is always a resonant process, in which those configurations whose band gaps match the excitation energy are preferentially excited. Any mixture of sp^3, sp^2 and sp^1 carbon atoms always has a gap between 0 and 5.5 eV, and this energy range matches that of IR-vis-UV Raman spectrometers [14]. We thus performed a resonant Raman study of the samples deposited at various fluences. The Raman spectra of carbons do not follow the vibration density of states, but consist of three basic features, the G and D peaks around 1600 and 1350 cm^{-1} and an extra T peak, for UV excitation, at ~1060 cm^{-1} [2,14]. The Raman spectra at any wavelength depend on 1) clustering of the sp^2 phase, 2) bond length and bond angle disorder, 3) presence of sp^2 rings or chains, and 4) the sp^2/sp^3 ratio. A two wavelength study (visible-UV) can however provide most of the information on the fraction and order of the sp^2 sites in amorphous carbon [14].

Visible Raman spectra for films deposited at different fluences are reported in Figure 1, and the corresponding UV Raman spectra in Figure 2. Figure 3 shows a comparison of the Raman spectra taken at different energies for

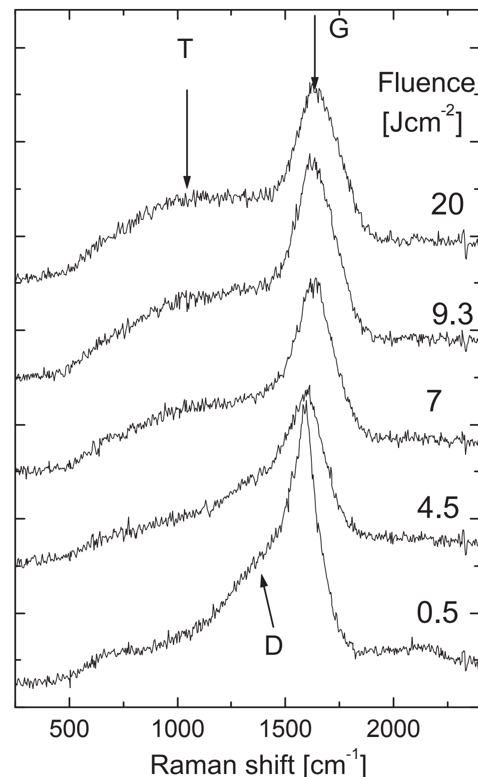

Fig. 2. 244 nm Raman spectra for a selection of samples grown at various fluences.

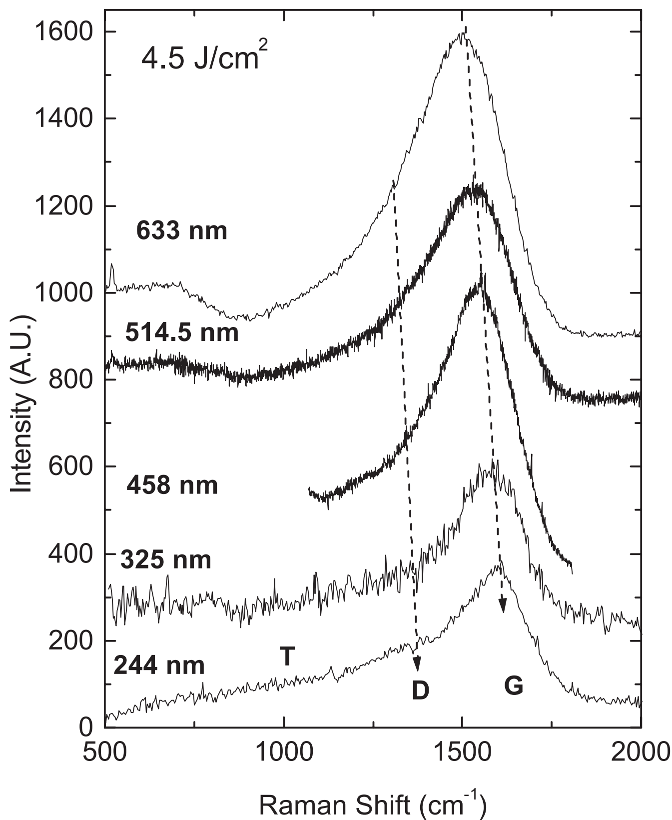

Fig. 3. Multi-wavelength Raman spectra for a sample grown at a fluence of 4.5 J cm^{-2}.

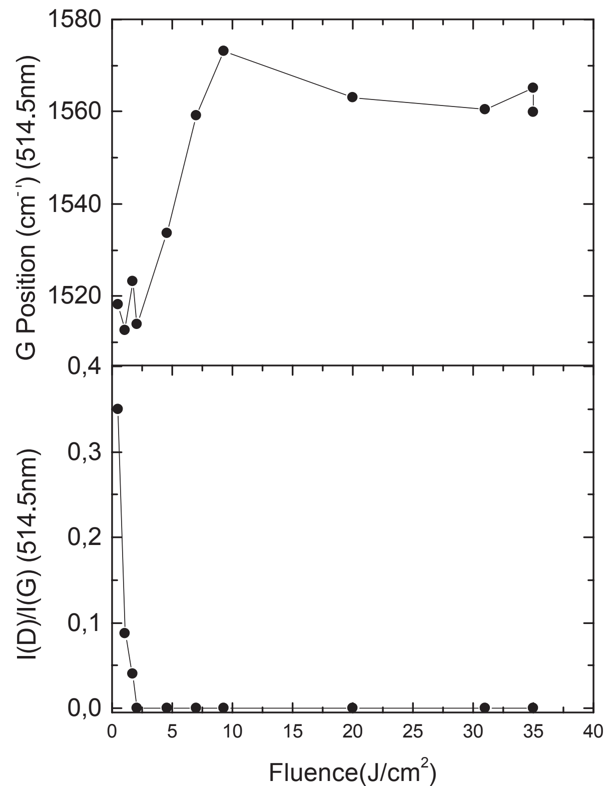

Fig. 4. Fitting parameters of 514.5 nm Raman spectra *versus* fluence: (A) G peak position, (B) Intensity ratio of G and D peaks, I(D)/I(G).

a film grown at 4.5 J cm^{-2}. Figures 1–3 suggest that the content of fourfold coordinated carbon changes with laser fluence. Two main features are evident for visible Raman spectra [2,18]: the D peak ($\sim$1350 cm^{-1}), due to breathing modes of rings, and the G peak ($\sim$1560 cm^{-1}) due to the relative motion of sp^2 carbon atoms [2]. In UV Raman spectra an extra T peak at $\sim$1060 cm^{-1} is evident. This peak is due to the resonant enhancement of σ bonds and directly probes the sp^3 bonding [14,19–21]. Figure 2 shows how for low fluences the T peak decreases and is replaced by an higher frequency residual D peak [14]. The combination of a Breit- Wigner-Fano (BWF) lineshape for the G-peak and a Lorentzian for the D (and T) peaks was used to fit the Raman spectra taken at the different excitation wavelengths ($\lambda = 229$, 244, 325, 458, 514.5, 633 nm). Note that we considered the Raman shift corresponding to the maximum (peak-value) of the BWF function, rather than to its centre, to allow comparison with literature data where symmetric lineshape fitting is used. The evolution of the main 514.5 nm and 244 nm Raman parameters with fluence is reported in Figures 4, 5.

The main information one gets from a multiwavelength study is the dispersion of the Raman peaks. Figure 6 shows the variation of the G position with excitation wavelength for some representative samples. Figure 7 shows the trend of the G peak dispersion (in cm^{-1}/nm) for samples grown at different fluences, obtained from a linear fit of the data

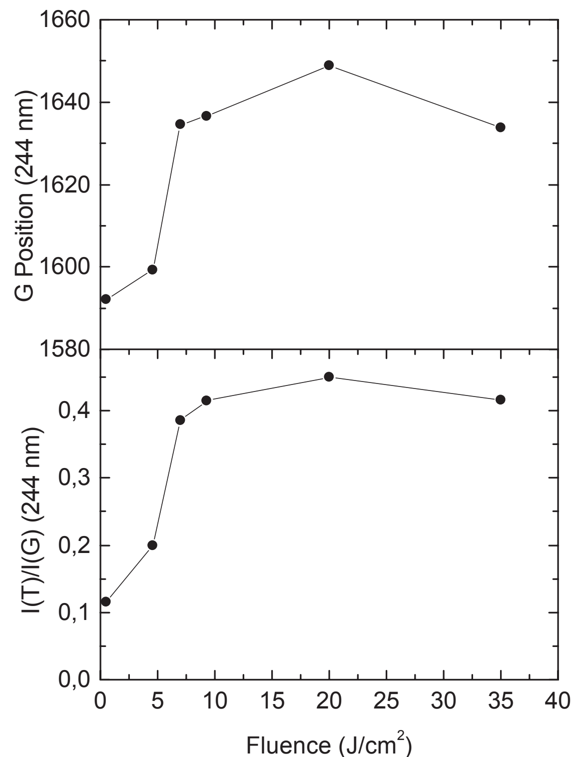

Fig. 5. Fitting parameters of UV-Raman spectra *versus* fluence: (A) G peak position, (B) Intensity ratio of the G and T peaks, I(T)/I(G).

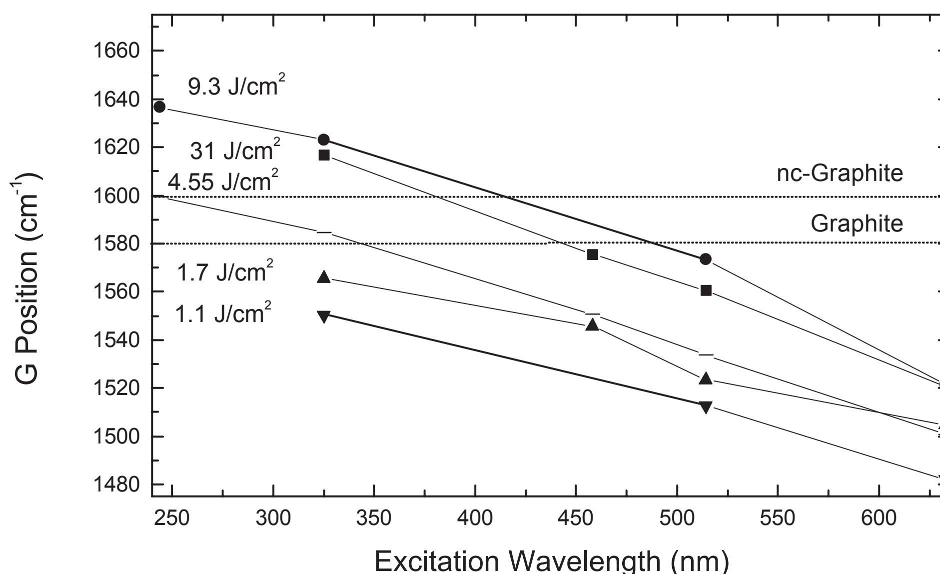

Fig. 6. Dispersion of the G peak *versus* excitation wavelength for a selection of samples grown at various fluences. For comparison, the non-dispersing G peak position of graphite at 1580 cm^{-1} and nano-crystalline graphite at ~1600 cm^{-1}, are indicated as a dotted line.

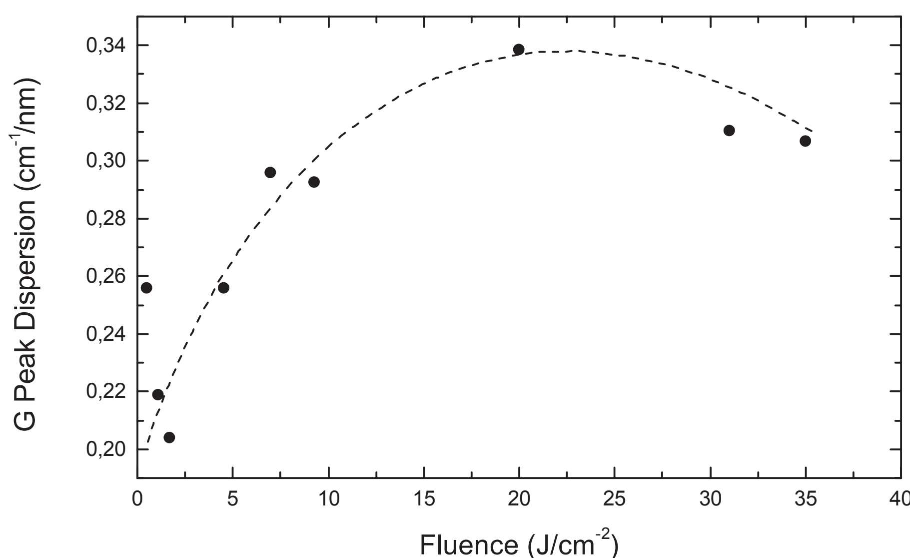

Fig. 7. G peak dispersion *vs.* laser fluence. The Y axis is the slope (in cm^{-1}/nm) of the linear fit of the G position *vs.* excitation wavelength data of Figure 6 and of the other samples not shown in Figure 6.

of Figure 6 and of the other samples not shown in Figure 6. In order to understand Figures 6, 7 we note that G peak does not disperse in graphite itself, nanocrystalline (nc)-graphite or glassy carbon [14]. The G peak only disperses in more disordered carbon, where the dispersion is proportional to the degree of disorder. This means that the physical behaviour of the G peak in disordered graphite is radically different from amorphous carbons, even though the G peak positions might accidentally be the same at some excitation energy. The G peak in graphite cannot disperse because it is the Raman-active phonon mode of the crystal. In nano-crystalline graphite, the G peak shifts slightly upwards at fixed excitation energy due to phonon confinement, but it cannot disperse with varying excitation energy, still being a density of states feature. The G peak dispersion occurs only in more disordered carbon, because now there are a range of configurations with different local band gaps and different phonon modes [14]. The dispersion arises from a resonant selection of sp^2 configurations or clusters with wider π band gaps, and correspondingly higher vibration frequencies. The G peak dispersion separates the materials into two types. In materials with only sp^2 rings, the G peak saturates at a maximum of ~1600 cm^{-1}, the G position in nc-graphite. In contrast, in those materials also containing sp^2 chains, particularly ta-C and ta-C:H, the G peak continues to

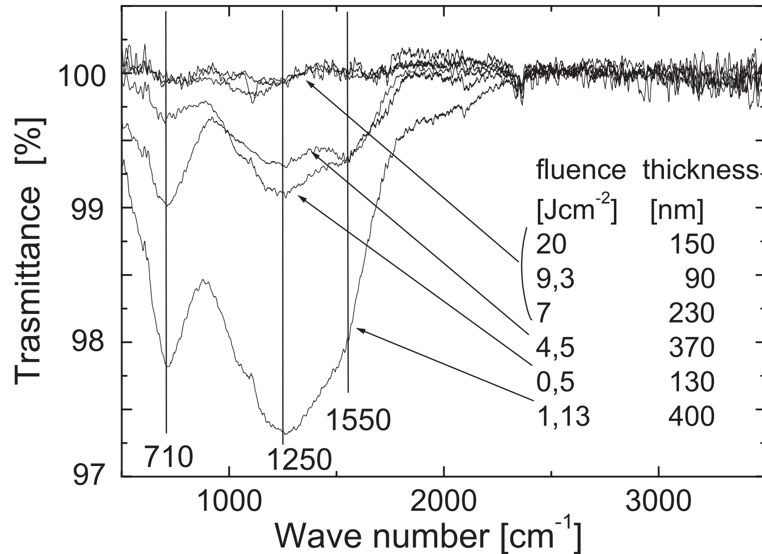

Fig. 8. FTIR transmission spectra for a selection of samples grown at various fluences. The main peaks are indicated.

rise past 1600 cm^{-1} and can reach 1690 cm^{-1} at 229 nm excitation in ta-C. Indeed, for visible excitation, sp^2 clustering and ordering will always *raise* the G peak for ta-C. In contrast, in UV excitation, increasing clustering *lowers* the G position, as noted above [14]. Thus the higher the dispersion, the lower the sp^2 clustering and, if combined with an I(T)/I(G) of at least 0.4, this is a sufficient condition to assert an sp^3 fraction of ∼70–80% or more [14,21].

The data in Figures 1–7 clearly show how above a threshold fluence (f_t) value of 5 J cm^{-2} the films consist largely of high sp^3 ta-C. We note that the simultaneous detection of an almost zero value for the I(D)/I(G) ratio and of a G peak position greater than 1550 cm^{-1} for visible Raman excitation is a sufficient condition to assert a high sp^3 content in the films [2]. Comparing films of similar thickness (*e.g.* films deposited at 0.5 J cm^{-2} and 20–30 J cm^{-2}, see Tab. 1), we observe that the intensity of the Si peaks from the substrate (I order at ∼520 cm^{-1} and II order at ∼970 cm^{-1}), increases with fluence. This again indicates greater transparency and hence is consistent with higher sp^3 content in the films deposited above the threshold f_t. Figures 5 and 7 directly confirm this observation, since they show I(T)/I(G) > 0.4 and an higher G peak dispersion for films grown at fluences higher than 5 J/cm^2. A closer inspection of Figure 7 shows that the G dispersion changes with fluence even for samples grown at high fluences, differently from the data of Figures 4 and 5. The fact that the film grown at 20 J/cm^{-2} has the strongest G dispersion shows that this film, although having a sp^3 content similar to the other higher fluence films, also has the lowest sp^2 clustering [2,14]. We also note that the maximum G dispersion (∼0.34 cm^{-1}/nm) is lower than the one reported for ∼88% sp^3 uniform ta-C films (∼0.44 cm^{-1}/nm) [14]. This means that our PLD ta-C films have more sp^2 clustering or cross-sectional layering than the S-bend FCVA ta-C analysed in reference [14]. Indeed cross sectional layering was detected by XRR, as described in Section 3.3. On the other hand the dispersion is minimum for $f < f_t$, thus indicating clustering of the sp^2 phase and lower sp^3 content in below-threshold films.

The low frequency Raman spectra of low fluence films show the low frequency double peak structure at about 400 and 800 cm^{-1}, typical of a-C samples [22–24], see Figure 1. This structure is lost, being replaced by a broadband centred at ∼600 cm^{-1}, for fluences above the threshold of 5 J/cm^2. This is typical of sp^2 bending modes in ta-C [25]. Here we discuss the attribution of the peak at ∼710 cm^{-1} shown in the inset of Figure 1. This peak coincides with a peak in the vibrational density of states of a graphene sheet [26,27]. The peak frequency is the same as that of the A_{2g} phonon at point M in the Brillouin Zone, which can be seen as a twisting motion of aromatic rings. The intensity of this peak was found to correlate to the intensity of the D peak [28], thus confirming that both modes are related to the presence of condensed aromatic sp^2 rings.

The analysis of the Raman spectra clearly shows the existence of a threshold fluence value around 5 J cm^{-2} for the deposition of ta-C films and this is confirmed by EELS measurements. EELS detected an sp^3 content ∼40% in the film deposited at 0.5 J cm^{-2}, consistent with the low I(T)/I(G), and of ∼80% in the film deposited at 20 J cm^{-2}. For the same samples X-ray reflectivity measurements gave bulk densities of 2–2.2 g cm^{-3} and 2.9–3 g cm^{-3} respectively, with presence of layers. Referring to Table 1, all films deposited at fluences below f_t show a *low* content of fourfold coordinated carbon, while in films deposited at fluences above f_t the sp^3 content is increasing up to 80%.

3.2 FTIR

Typical FTIR transmission spectra of PLD films on Si are reported in Figure 8. Three broad bands are visible in the spectra of films deposited at fluences below f_t: the first, at

$\sim$710 cm^{-1}, corresponds to the feature seen in the Raman spectra and previously discussed. The second is composed of a peak at about 1250 cm^{-1} and a high frequency shoulder at about 1550 cm^{-1}. No evidence of the above bands is present in the spectra of the films deposited above f_t, which are transparent, thus confirming that with increasing fluence a structural transition from low sp^3 carbon to ta-C occurs. The lack in all spectra of absorption bands in the range 2800–3100 cm^{-1}, due to the C-H$_x$ stretching modes, indicates that our films are hydrogen free (H content is lower than the detectable limit of 0.5at.%).

Although a full interpretation of the IR spectrum is not yet possible, Figure 8 allows us to reach some conclusions. Comparing Figure 8 and Figures 1–3 it is clear that the FTIR spectra do not resemble the Raman spectra at any of wavelength we used. Indeed, given that Raman spectroscopy in carbons is always a resonant process and that the shape and intensity of the peaks change with excitation energy, the similarity between the FTIR spectra and green Raman spectra of certain amorphous carbons is accidental [28]. However, the fact that in all kind of amorphous carbons the IR spectrum mainly shows two broad bands in the 1300 and 1600 cm^{-1} region could suggest that a link between these bands and the vibrations responsible for the Raman D and G peak should be present. Figure 8 shows that the intensity of these bands in pure carbon samples is related to the decrease in the sp^3 fraction. A higher fraction of the sp^2 phase and higher electron delocalisation allows higher charge fluxes and thus higher IR activity. We can assume that the more delocalised sp^2 phase is responsible for the vibrational modes seen in the FTIR spectra. Indeed, in the case of ta-C, the localisation of the sp^2 phase is maximum and no features in FTIR spectra are detected. One could assume that the sp^2–sp^3 bonds generate a dipole that should give IR active vibrations. However, first it is highly doubtful that the sp^2–sp^3 hybridisation alone can give rise to a polarisation degree sufficient to make the system IR active, and, second, if this were the case, samples with the maximum content of sp^2–sp^3 bonds should give the highest signal. However, this is not, since the spectrum observed for sputtered a-C [28] shows the same overall features of the spectra of our films prepared at low fluences (Fig. 8) and of a-C:H samples annealed at high temperature. Furthermore no new bands appear in the spectra of high sp^3 (>40%) samples in Figure 8, which should have the biggest number of mixed bonds.

The more delocalised sp^2 phase is detected in the Raman spectra at the lowest excitation energy [2,14]. It is thus conceivable that the IR spectra should be comparable with the non-resonant Raman spectra in the ideal null-excitation energy experimental configuration. Both 0 energy Raman and IR spectra would probe the same, most delocalised sp^2 phase and this links the two measurement techniques. Thus the 1550 cm^{-1} band will have a stretching character both in Raman and IR spectra and the $\sim$1250 cm^{-1} band will comprise also a bending character, although the symmetry of the modes giving rise to these two broad bands in IR and Raman spectra might be different. Indeed, for ordered poly-aromatic hydrocarbons (PAH) the same normal modes are not responsible for both IR and Raman features. This is supported by experiments and density functional theory calculations [30] on vibrational spectra of model sp^2 coordinated systems, such as the C_{114} and C_{222}. In these highly symmetric D_{6h} tiles hydrogen does not significantly affect vibrational spectra (no features are observed in the 1400–1600 cm^{-1} region, which could be attributed to C-H modes): both molecules show structured IR bands both around 1250 cm^{-1} and 1550 cm^{-1}. These are due to highly cooperative motions of the molecule as a whole, involving combinations of C-C stretching and bending. Yet these molecules do have an inversion centre and, as such, selection rules forbid any Raman feature at the same frequencies [31]. On the other hand, when disorder is present, such as in our films, FTIR spectra and the ideal non- resonant Raman spectra could be more strictly correlated.

3.3 X-ray reflectivity

XRR can provide information on density, roughness and cross-sectional layering of amorphous carbons, without any sample preparation or damage [15,32–37]. The refractive index for X-rays in solids is smaller than unity, so that total external reflection occurs at low angles of incidence. As the incidence angle θ_i increases above a critical angle θ_c, X-rays start to penetrate into the film. From Snell's law at the air/film interface, one can obtain the critical angle for a medium composed by a single element:

$$\theta_c = \lambda \sqrt{\frac{N_A r_0}{\pi} \rho \frac{(Z + f')}{M}} \qquad (1)$$

where r_0 is the classical electron radius, N_A is the Avogadro number, f' takes dispersive corrections into account, ρ is the mass density, Z and M are the element atomic number and atomic mass respectively. For carbon, at $\lambda = 1.3926$ Å, $f'_C \approx 10^{-2}$. Thus from the critical angle we can obtain the density of a material composed of carbon only [15]:

$$\rho \cong 2 \frac{\pi^2 c^2 \varepsilon_0}{3\lambda^2 N_A e^2} M_C m_e \theta_c^2 \qquad (2)$$

where m_e is the electron mass.

When a thin layer is deposited on a substrate, X-rays reflected at the film surface and at the film-substrate interface can interfere and from Snell's law, one can see that constructive interference produces fringes in the reflectivity curve. Thickness can thus be found from the fringe period. XRR also probes atomic scale surface roughness, which results in X-rays being scattered out of the specular beam. By fitting the XRR data to simulated curves a model reproducing the material parameters can be obtained. Simulations were performed using the Bede REFS-MERCURY software package, which uses Parrat's recursive formalism of the Fresnel equations to calculate the reflected wave amplitude and, hence, the reflected intensity [36,38–40].

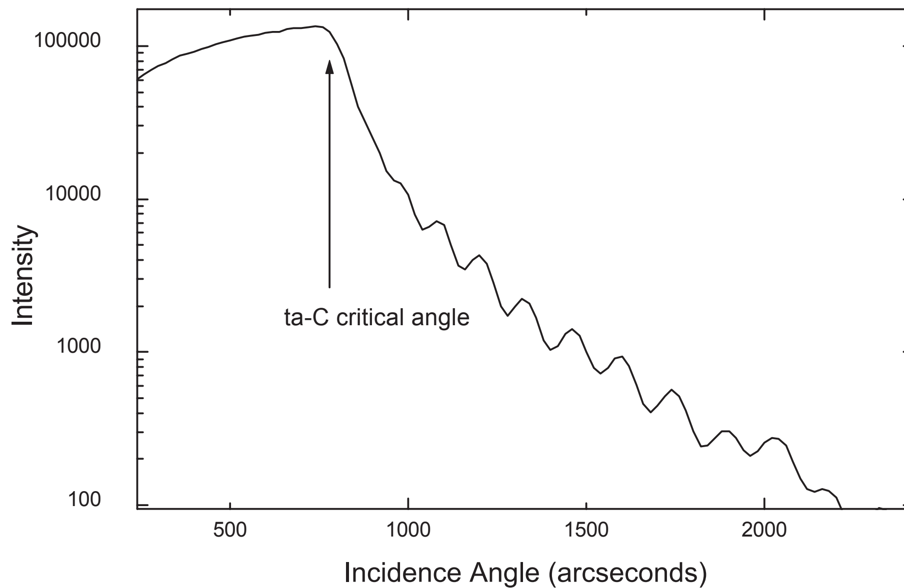

Fig. 9. Critical angle in the reflectivity curve of a film grown at 9.3 J cm^{-2}. The corresponding density is 2.88 g/cm^3.

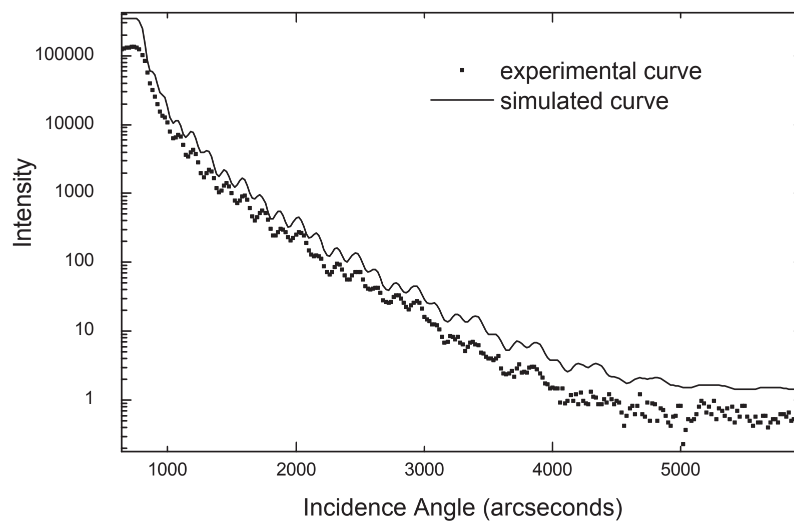

Fig. 10. Reflectivity profile of a film grown at a fluence of 9.3 J cm^{-2} ; the upper line, shifted for clarity, is a simulation for a film with structure:

	Density (g cm^{-3})	thickness (nm)	r.m.s roughness (nm)
Si			
C	2.47	6	0.8
C	2.88	58.5	1
C	2.74	30.5	0.85

If the material density is smaller than, or comparable to the Si substrate density ($\rho = 2.33$ g/cm^3), the X-rays are reflected at the Si surface and so the Si critical angle is seen, rather than that of the film, which only perturbs the shape of the substrate critical angle. In this situation, we have to simulate the shape of the critical angle thus obtaining broader error bands for the calculated density. This is the case of a film deposited below threshold (fluence = 1.13 J cm^{-2}) for which we obtained a density value of ~2.0–2.2 g cm^{-3}. For the same reason, if a film consists of a bulk dense layer with thinner and less dense layers at the top and the bottom, the critical angle is that of the bulk layer [15]. Thus, from the critical angle (see Fig. 9), we directly get the density of the densest layer and not the average film density, that requires a fit of the multilayer structure. This is the case for the film deposited above f_t: from the experimental critical angle, we found a bulk density of ~3.0 g cm^{-3} for the samples deposited at 20–30 J cm^{-2}, and of ~2.9 g cm^{-3} for a fluence value of ~9.3 J cm^{-2}. This last sample was the one giving the best reflectivity curve shown in Figures 9, 10. The different periodicities indicate internal layering, and

the curve could be simulated considering three layers with different densities (see Fig. 10). The number of layers, their density, thickness and roughness are all variable parameters and the density within the layers is probably not constant, which introduces further uncertainty in the simulated parameters. The overall thickness, the surface layer thickness and the bulk layer density can be considered the most reliable fitted data (see caption of Fig. 10). Layering in PLD films was previously reported for pulsed laser deposited ta-C, by cross-sectional High Resolution TEM measurements [5]. For samples deposited at higher fluences (20 and 30 J cm^{-2}) only a weak periodicity corresponding to a top layer of $\sim$30 nm is present in the measurement, while no fringes at all could be detected in the sample deposited below f_{t}. The absence of fringes for low fluence samples could be due to the thickness inhomogeneity of the films. This problem is more important if the films are very thick, as in this case (see Tab. 1) and so the detected periodicity probably indicates a surface layer with a different density. The top surface r.m.s. roughness was found to be less than 1 nm for the samples examined with XRR.

Note that the maximum density of our films is smaller than the maximum density of $\sim$3.26 g/cm^3 detected for very uniform S-bend FCVA films [15]. This is in agreement with the observation that the maximum dispersion of the G peak in our films is lower than the G peak dispersion in S-bend FCVA films.

3.4 Internal stress

The macroscopic stress was obtained by comparing the substrate curvature before and after film deposition and applying the Stoney's equation (Tab. 1). Stresses are compressive and increase with fluence, but they are always lower than 2 GPa. This is the lowest value reported to date for as deposited ta-C, with no B [41], or Si introduction [42], post deposition annealing [7,43], or soft interface layer [44]. In fact the usual range of macroscopic stresses in as deposited ta-C films is of the order of 10 GPa [45–47]. In films deposited at fluences below f_{c}, with thickness up to more than 1 micron, the residual stress is very low (around 0.5 GPa). In high sp^3 films the stress is nearly independent of film thickness, within our thickness range, between 90 and 230 nm. Also, the presence of a ceramic interlayer appears not to affect the residual stress value. Note that the G peak position in our relatively low stress films is comparable with the one of highly stressed films. This confirms that the high G peak position in ta- C films is due to the presence of short sp^2 chains and not to the high stress [2].

3.5 Nano indentation

Hardness values for films deposited at various fluences are reported in Table 1. In the films deposited on Si, hardness increases with fluence up to values of 40 GPa. Since the harder films are not thicker than 130 nm and the indentation depth is 50 nm, film hardness is certainly underestimated due to the influence of the comparatively soft substrate. Indeed it is not possible to detect a threshold fluence value for the measured hardness, but a smooth trend of increasing hardness with increasing fluence. Taking in account the bigger thickness of the low fluence films we can assume that this smooth trend is due to the greater influence of the substrate for the thinner films grown at higher fluences. This also means that 30–35 GPa is a genuine hardness value for the low fluence films. Table 1 also shows that the hardness of high fluence ta-C films deposited on Si+SiC rises to 65–70 GPa. The harder SiC interface layer has thus reduced the substrate effect.

The best way to non destructively determine the elastic constants of thin films is using surface acoustic waves based methods, such as surface Brillouin scattering [48] or laser induced surface acoustic waves [6]. The relation between Young's modulus and coordination derived in reference [48] for amorphous carbon would give a Young's modulus of $\sim$330 GPa for $\sim$40% sp^3 films and $\sim$630 GPa for $\sim$80% sp^3 films. These would correspond to hardness of $\sim$33 and 63 GPa respectively, according to the relation between hardness and Young's modulus in amorphous carbons, $E/H \approx 10$ [49]. This agrees with our conclusion that the hardness given by nanoindentation is a good measure for thick films deposited at low fluences and that the addition of the harder SiC interface allows good estimates of the hardness of thin high fluences films.

3.6 Scratch test

Table 1 shows that for films deposited on Si the upper critical load LC2 increases with both laser fluence and film thickness. LC2 is defined as the load for which the film is completely removed from the scratch path [50]. As a rule, films deposited above f_{t}, with thickness higher than 100 nm, show LC2 between 16 and 20 N, corresponding to a maximum Hertzian contact pressure $p_{\max}$ around 16 GPa; these values for LC2 and $p_{\max}$ are higher than those reported for single layer ta-C films 500 nm thick, deposited on 440 steel (LC2 $\sim$ 10 N, $p_{\max} \sim$ 1 GPa) [51,52]. In our films LC2 values are lower than 4 N for Si+TiN, around 10 N for Si+TiC and around 15 N for Si+SiC. Such results do not necessarily mean that ta-C films deposited on ceramics show adhesion and load supporting capacity worse than those of films deposited on Si. Harder substrates sink-in less under the indenter, so that stress and strain distributions in the film and at the interface are modified. Scanning Electron Microscopy (SEM) images of scratches corresponding to LC2s indicate that scratch diameters are larger in films deposited on Si than on Si+SiC. Notwithstanding the different LC2 values, $p_{\max}$ is comparable in the two kinds of film. Scratch tests indicate that ta-C adhesion to Si+SiC is better than to Si and to Si+TiC (the two are equivalent to each other with respect to adhesion, but Si+TiC is more suitable for mechanical applications); ta-C adhesion to TiN is poor.

Friction coefficients, as deduced from scratch tests in ambient humidity, vary between 0.11 and 0.06, and are in general lower than 0.08 (Tab. 1). This is consistent with previously reported data for the ambient humidity ball-on-disk measurements on PLD ta-C films [53].

4 Discussion

The existence of a threshold fluence f_t at which the film structure changes from graphitic to diamond-like can be traced to a corresponding threshold in the values of ablated particle energy. Indeed, according to literature data [54,55] the detected species in the plume produced by laser irradiation of graphite mainly consist of C, C_2, C^+ and C^{++}, where the C_2 component is most probably produced through ion-atom collisions followed by charge neutralisation in the plume [55]. What is relevant in ta-C formation is the energy of the C^+ ions impinging on the growing C film, which will be graphitic if only neutral, low energy carbon atoms arrive on the substrate. A C^+ energy exceeding ~100 eV is usually considered a necessary condition to obtain a high sp^3/sp^2 bond ratio [45]. Indeed, we observed ta-C formation in our films whenever the laser fluence exceeded f_t, as expected taking into account that the energy of C^+ ions is an increasing function of laser fluence (see Tab. 2 of Ref. [54]). Given the strong similarity between experimental conditions, we assume the same energy values of plume particles as in [54], which was measured to be 120, 175 and 440 eV for fluences of 7, 30 and 200 J/cm^2 at a pressure of 5×10^{-3} Pa. Also, a short laser wavelength makes the plasma plume, including atomic and ionic species, much energetic and highly ionised [56]. This explains why, by using lasers such as KrF and ArF (193 nm), amorphous carbon films with a high sp^3/sp^2 bond ratio have been successfully deposited even at relatively low laser energy densities compared with the PLD at longer laser wavelength [56].

Let us now make a few further considerations about C^+ ions impinging on a growing carbon film. All energetic particles penetrate into the film and are stopped at different depths, increasing with their energy, in interstitial positions. According to SRIM simulations [57] 50, 100 and 175 eV particles are stopped within 0.5, 1.5 and 2.2 nm below the surface. Besides, each most energetic ion (175 eV) produces 1.5 recoils; thus the thermal spike model to explain ta-C formation [58] is ruled out for our energy range, simply because dense cascades do not form. The subplantation model predicts film densification, and transition from sp^2 to sp^3 coordination, with a maximum usually identified around 100 eV [59]. As already pointed out, residual stresses as high as 10 GPa, or more [45–47] have been measured in ta-C films; on such a basis it was postulated [47] that high compressive local stresses are *necessary* to obtain ta-C films. However, the fact that, *e.g.*, post deposition thermal annealing releases the stress without appreciable change in the sp^3 fraction, shows that high stresses are just the by-product of the energetic deposition process [7,43,60]. Indeed, in our ta-C films we measured relatively low residual stresses of 2 GPa, at most (see Tab. 1). A possible explanation for this low stress is that the stress self-annealing is prompted by low energy particles. Below f_t, the mechanism is most effective (see Tab. 1), but the sp^3 fraction is lower; above f_t residual stresses increase because energetic C^+ give rise to a higher degree of stress, while the low energy plume component is unable to completely relax it. This would support the idea that the dominant mechanism in film formation by PLD involves a delicate balance between the number density and energy of charged and neutral particles. Thus also PLD belongs to the family of beam assisted deposition processes [60]. On the other hand the heavy layering present in these films, as shown by XRR, could contribute to stress lowering. Furthermore our relatively high pressure leads to a lower average ion energy with respect to the other PLD deposited ta-C films [61], thus resulting in a lower stress. A deeper investigation is needed to understand the stress release mechanism in our as- deposited films, the ultimate target being the deposition of fully stress free ta-C films, without any additional treatment. The main result we wish to underline is that we clearly showed that the macroscopic stress is definitely not inducing the formation of the sp^3 phase, contrary to what previously stated [47].

The threshold fluence we found corresponds to a power density of 2.5×10^8 Wcm^{-2} [62] slightly below the limit of 3×10^8 Wcm^{-2} reported for the same laser wavelength [11,63]. It should be noted that we obtained ta-C films with a simple configuration of the deposition system, without any additional energy source. This result is significant because our films were deposited in a vacuum considerably worse than that sometimes suggested as necessary to obtain ta-C [4,9].

5 Conclusions

We grew by Pulsed laser deposition and characterised ta-C films on Si both with and without a carbide interlayer, working in a vacuum of 10^{-2} Pa. Structural characterisation showed the existence of a threshold fluence of ~5 J cm^{-2}, above which the films largely consist of ta-C. Our as deposited 80% sp^3 films have low macroscopic stresses (<2 GPa), an hardness of 70 GPa and a friction coefficient in ambient humidity lower than 0.1. The better adhesion properties are shown by ta-C on SiC. We showed how a multi-wavelength Raman investigation is able to reveal the quantity and quality of the sp^2 phase and thus fully characterise the bonding structure. We also pointed out how the FTIR activity in pure carbon films is correlated with the increasing delocalisation of the sp^2 phase and is thus highest in low sp^3 films. We proved how the introduction of an harder SiC interface layer allows reliable nanointentation measurements in thin ta-C films.

The authors are grateful to Prof. D. Batchelder of Leeds University, to Dr. M. Kuball of Bristol University, to Prof. M. Stutzmann of Walter Schottky Institute Muenchen, to Dr. D. Richards and to Dr. G. Gibson of Cambridge University for

the access to Raman facilities, to S.E. Rodil and V. Stolojan of Cambridge University for EELS measurements. This work has been funded by CNR-Progetto Finalizzato Materiali Speciali per Tecnologie Avanzate II and by MURST under project COFIN 99. A.C.F. acknowledges funding from an E.U. TMR Marie Curie fellowship.

References

1. J. Robertson, Progr. Solid State Chem. **21**, 199 (1991); Pure Appl. Chem. **66**, 1789 (1994); Adv. Phys. **35**, 317 (1986).
2. A.C. Ferrari, J. Robertson, Phys. Rev. B **61**, 14095 (2000).
3. C.L. Marquardt, R.T. Williams, D.J. Nagel, Mater. Res. Soc. Symp. Proc., Vol. **38**, 325 (1985).
4. D.L. Pappas, K.L. Saenger, J. Cuomo, R.W. Dreyfus, J. Appl. Phys. **72**, 3966 (1992).
5. M.P. Siegal, J.C. Barbour, P.N. Provencio, D.R. Tallant, T.A. Friedmann, Appl. Phys. Lett. **73**, 759 (1998).
6. D. Schneider, C.F. Meyer, H. Mai, B. Shoneich, H. Ziegle, H.J. Sheibe, Y. Lifshitz, Diamond Relat. Mater. **7**, 973 (1998).
7. T.A. Friedmann, J.P. Sullivan, J.A. Knapp, D.R. Tallant, D.M. Follstaedt, D.L. Medlin, P.B. Mirkarimi, Appl. Phys. Lett. **71**, 3820 (1997).
8. A.A. Puretzky, D.B. Geohegan, G.E. Jellison, M.M. McCulloch, Appl. Surf. Sci. **96-98**, 859 (1996).
9. S.J.P. Laube, A.A. Voevodin, Surf. Coat. Techn. **105**, 125 (1998).
10. K. Yamamoto, Y. Koga, S. Fujiwara, E. Kokai, R.B. Heinmann, Appl. Phys. A **66**, 115 (1998).
11. A.A. Voevodin, M.S. Donley, Surf. Coat. Techn. **82**, 199 (1996).
12. R.F. Haglund, Mechanism of Laser desorption and ablation in Laser Ablation and Desorption, edited by J.G. Miller, R.F. Haglund (Academic Press, 1998).
13. M. Bonelli, C. Cestari, A. Miotello, Meas. Sci. Technol. **10**, 27 (1999).
14. A.C. Ferrari, J. Robertson, Phys. Rev. B **64**, 075414 (2001); Phys. Rev. B **63**, 121405(R) (2001).
15. A.C. Ferrari, A. Li Bassi, B.K. Tanner, V. Stolojan, J. Yuan, L.M. Brown, S.E. Rodil, B. Kleinsorge, J. Robertson, Phys. Rev. B **62**, 11089 (2000).
16. M. Ohring, *The Materials Science Of Thin Films*, Chap. 9 (Academic Press, 1992).
17. G.M. Pharr, W.C. Oliver, MRS Bulletin **7**, 1564 (1992).
18. S. Prawer, K.W. Nugent, Y. Lifshitz, G.D. Lempert, E. Grossman, J. Kulik, I. Avigal, R. Kalish, Diamond Relat. Mater. **5**, 433 (1996).
19. K.W.R. Gilkes, H.S. Sands, D.N. Batchelder, J. Robertson, W.I. Milne, Appl. Phys. Lett. **70**, 1980 (1997).
20. V.I. Merkulov, J.S. Lannin, C.H. Munro, S.A. Asher, V.S. Veerasamy, W.I. Milne, Phys. Rev. Lett. **78**, 4869 (1997).
21. K.W.R. Gilkes, S. Prawer, K.W. Nugent, J. Robertson, H.S. Sands, Y. Lifshitz, X. Shi, J. Appl. Phys. **87**, 7283 (2000).
22. F. Li, J.S. Lannin, Appl. Phys. Lett. **61**, 2116 (1992).
23. Q. Wang, D.D. Allred, J. Gonzalez-Hernandez, Phys. Rev. B **47**, 6119 (1993).
24. F. Parmigiani, E. Kay, H. Seki, J. Appl. Phys. **64**, 3031 (1988).
25. W.S. Bacsa, J.S. Lannin, D.L. Pappas, J.J. Cuomo, Phys. Rev. B **47**, 10931 (1993).
26. R. Al.-Jishi, G. Dresselhaus, Phys. Rev. B **26**, 4514 (1982).
27. C. Mapelli, C. Castiglioni, G. Zerbi, K. Müllen, Phys. Rev. B **60**, 12710 (1999).
28. S.E. Rodil, A.C. Ferrari, J. Robertson, W.I. Milne, J. Appl. Phys. **89**, 5425 (2001).
29. M.L. Theye, V. Paret, A. Sadki, Diamond Relat. Mater. **10**, 182 (2001).
30. C. Castiglioni, C. Mapelli, F. Negri, G. Zerbi, J. Chem. Phys. **114**, 963 (2001).
31. E. Meroni, *Adv. School on Polymer Science Thesis*, Politecnico di Milano (1999).
32. F. Toney, S. Brennan, J. Appl. Phys. **66**, 1861 (1989).
33. A. Lucas, T.D. Nguyen, J.B. Kortright, Appl. Phys. Lett. **59**, 2100 (1991).
34. S. Logothetidis, G. Stergioudis, Appl. Phys. Lett. **71**, 2463 (1997).
35. Q. Zhang, S.F. Yoon, Rusli, J. Ahn, H. Yang, D. Bahr, J. Appl. Phys. **86**, 289 (1999).
36. B. Lengeler, *X-Ray Absorption and Reflection in the Hard X-Ray Range*, edited by M. Campagna, R. Rosei (North Holland, 1990).
37. A. LiBassi, A.C. Ferrari, V. Stolojan, B.K. Tanner, J. Robertson, L.M. Brown, Diamond Relat. Mater. **9**, 711 (1999).
38. L.G. Parrat, Phys. Rev. **95**, 354 (1954).
39. M. Wormington, I. Pape, T.P.A. Hase, B.K. Tanner, D.K. Bowen, Phil. Mag. Lett. **74**, 211 (1996).
40. S.K. Sinha, E.N. Sirota, S. Garoff, Phys. Rev. B **38**, 2297 (1988).
41. M. Chhowalla, Y. Yin, G.A.J. Amaratunga, D.R. McKenzie, T. Frauenheim, Appl. Phys. Lett. **69**, 2344 (1996).
42. J. Meneve, E. Dekempeneer, J. Smeets, Diamond Films Technol. **4**, 23 (1994).
43. A.C. Ferrari, B. Kleinsorge, N.A. Morrison, A. Hart, V. Stolojan, J. Robertson, J. Appl. Phys. **85**, 7191 (1999).
44. A. Anttila, L. Lappalainen, V.M. Tiainen, M. Hakovirta, Adv. Mater. **9**, 1161 (1997).
45. P.J. Fallon, V.S. Veerasamy, C.A. Davis, J. Roberston, G.A.J. Amaratunga, W.I. Milne, Phys. Rev. B **48**, 4777 (1993).
46. X. Shi, D. Flynn, B.K. Tay, S. Prawer, K.W. Nugent, S.R.P. Silva, Y. Lifshitz, W.I. Milne, Phil. Mag. B **76**, 351 (1997).
47. D.R. McKenzie, D. Muller, B.A. Pailthorpe, Phys. Rev. Lett. **67**, 773 (1991).
48. A.C. Ferrari, J. Roberston, M.G. Beghi, C.E. Bottani, R. Ferulano, R. Pastorelli, Appl. Phys. Lett. **75**, 1893 (1999).
49. J. Robertson, Surf. Coat. Technol. **50**, 185 (1992).
50. *Advanced Surface Coatings: a Handbook of Surface Engineering*, edited by D.S. Rickerby, A. Matthews (Blackie, Glasgow and London, 1991), p. 331.
51. A.A. Voevodin, M.S. Donley, J.S. Zabinski, Surf. Coat. Technol. **92**, 42 (1997).
52. A.A. Voevodin, M.S. Donley, J.S. Zabinski, J.E. Bultman, Surf. Coat. Technol. **76-77**, 534 (1995).
53. A.A. Voevodin, A.W. Phelps, J.S. Zabinski, M.S. Donley, Diamond Relat. Mater. **5**, 1264 (1996).

54. B. Angleraud, J. Aubreton, A. Catherinot, Eur. Phys. J. AP **5**, 303 (1999).
55. Y. Yamagata, A. Sharma, J. Narayan, R.M. Mayo, J.W. Newmann, K. Ebihara, J. Appl. Phys. **86**, 4154 (1999).
56. A.A. Voevodin, S.J. Laube, S.D. Walck, J.S. Solomon, M.S. Donley, J.S. Zabinsky, J. Appl. Phys. **78**, 4123 (1995).
57. J.F. Ziegler, J.P. Biersack, *The Stopping and Ranges of Ions in Matter*, SRIM- 2000.10.
58. H. Hofsäss, H. Feldermann, R. Merk, M. Sebastian, C. Ronning, Appl. Phys. A **66**, 153 (1998).
59. Y. Lifshitz, S.R. Kasi, J.W. Rabelais, Phys. Rev. Lett. **62**, 1290 (1989).
60. M. Bonelli, A.P. Fioravanti, A. Miotello, P.M. Ossi, Europhys. Lett. **50**, 501 (2000).
61. Y. Lifshitz, Diamone Relat. Mater. **5**, 388 (1996).
62. M. Bonelli, A.C. Ferrari, A.P. Fioravanti, A. Miotello, P.M. Ossi, Mater. Res. Soc. Symp. Proc. **593**, 359 (2000).
63. F. Müller, K. Mann, Diamond Relat. Mater. **2**, 233 (1993).